RSC Advances

ROYAL SOCIETY OF CHEMISTRY

www.rsc.org/advances

A sol-gel derived, copper-doped, titanium dioxide-reduced graphene oxide nanocomposite electrode for the photoelectrocatalytic reduction of CO_2 to methanol and formic acid

Md. Rakibul Hasan[a,1], Sharifah Bee Abd Hamid[b,1], Wan Jeffrey Basirun[c,2], Syazwan Hanani Meriam Suhaimy[d,1], Ahmad Nazeer Che Mat[e,2]

[1]Institute of Nanotechnology & Catalysis Research (NanoCat), 3rd Floor, Block A, Institute of Postgraduate Studies (IPS), University of Malaya, 50603 Kuala Lumpur, Malaysia.

[2]Department of Chemistry, Faculty of Science, University of Malaya, 50603 Kuala Lumpur, Malaysia.

E-mail: [a]rakibacctdu@gmail.com; [b]sharifahbee@um.edu.my; [c]jeff@um.edu.my; [d]hanani_ms@yahoo.com.my; [e]hmd_naz@yahoo.com

*corresponding author: rakibacctdu@gmail.com

Abstract

Classic Cu-RGO-TiO_2 photoelectrocatalyst was fabricated by a facile sol-gel method, deposited on ITO film via electrophoretic deposition and characterized by XRD, FESEM, UV-Vis and FT-IR spectroscopy. A uniformly distributed porous composite film was observed on the ITO substrate with an average particle size of 18 nm. A lower photoluminescence response of the Cu-RGO-TiO_2 sample indicates better electron/hole separation upon irradiation. A maximum 1.31 mA cm^{-2} photocurrent density was observed at -0.61 V bias potential under solar simulator irradiation during CO_2 photoelectrocatalysis. Formic acid and methanol were the main products, but longer reaction times led to an increased methanol formation. The estimated current

efficiency of the production of formic acid and methanol was 32.47%, and the estimated rates of formation of formic acid and methanol were 255 μmol h^{-1} cm^{-2} and 189.06 μmol h^{-1} cm^{-2}, respectively.

Keywords: Reduced graphene oxide, titanium, carbon dioxide reduction, photoelectrochemistry, photoelectrocatalysis.

1. Introduction

The recycling of greenhouse gases (i.e., CO_2 and CH_4) offers long term solutions for energy and environmental related problems [1]. The presence of excess carbon dioxide (CO_2) in the earth's atmosphere has a great negative impact which is the warming of the planet. Various methods have been developed to efficiently convert and recycle CO_2. Renewable energy can be utilized in the CO_2 recycling process because it is a valuable raw material for the production of combustible chemicals such as formic acid, methanol and methane [2, 3]. CO_2 photoconversion is challenging for several reasons: inefficient absorption of visible light by present day photocatalysts, low quantum efficiency due to rapid e^-/h^+ recombination upon irradiation, facile backward redox reactions that lead to product dissociation and lack of product selectivity. These disadvantages are the main obstacles for the commercial success of CO_2 recycling [4].

However, current markets for CO_2-based products are developing, rather than considering it a waste chemical. Photoelectrocatalytic reduction of CO_2 is able meet this high energy conversion demand by utilizing free and abundant solar energy [5]. Successful conversion of CO_2 depends on a highly active photocatalyst or photoelectrocatalysis that can facilitate high rates of conversion while drastically decreasing the necessary energy input [6].

The earliest report of CO_2 photoconversion was published by Halmann in 1978 [7]. Honda and Fujishima first reported the use of titanium dioxide in the photoelectrolysis of water, but did not report the photoreduction of CO_2 with titanium until 1979 [8]. Since that time, TiO_2 has remained the most preferred photocatalyst and photoelectrocatalyst for CO_2 reduction. TiO_2 nanoparticles doped with N, Pt, Ag and Cu, among others, exhibited significant CO_2 photoconversion [9-11]. The wide band gap (i.e., 3.2 eV for the anatase phase) of TiO_2 is favorable due to its strong redox ability and high resistance to photocorrosion. Metal doping of TiO_2 could decrease the recombination process because the metal centers function as electron traps. Moreover, due to the work function difference, a Schottky barrier appears in the bimetallic TiO_2 structure. This phenomenon also helps to decrease the recombination of charge carriers [9]. TiO_2 structures incorporated with crystalline carbon structures, such as graphene, reduced graphene oxide (RGO) and carbon nanotubes, exhibit high catalytic efficiencies [11-13]. Graphene-TiO_2 composite materials have been described as future generation photocatalysts due to the low toxicity and extended photoactivity [14, 15]. Carbon structures can also promote simple reaction mechanisms during catalysis, which result in higher selectivity and desired yields [16]. Thus, further modification of the TiO_2 nanostructures can enhance the overall photoconversion of CO_2.

Reduced graphene oxide (RGO) as a catalyst promoter with TiO_2 was reported in our previous work [17]. Composite photocatalysts consisting of several elements are promising materials for visible light activity which enhance the kinetic properties of the desired reactions [18]. Mohamed *et al* reported RGO-TiO_2 composites for the photocatalytic reduction of CO_2 to methane gas [19]. They reported that the incorporation of the RGO into the composite increased

the photocatalytic performance of TiO_2 compared to pure TiO_2 by decreasing the TiO_2 band-gap into the visible region and prolonging the recombination time of the charge carriers [19]. On the other hand, Cu is a representative d-block element with attractive catalytic properties for CO_2 electroreduction process. Copper electrodes have shown great success in hydrocarbon gas production such as hydrogen (H_2), methane (CH_4) etc. Moreover, the Cu atoms can act as a channel for the dispersion of photoelectrons, which suppress the e^-/h^+ recombination in the photoelectrocatalysis process. Hence, a Cu-RGO-TiO_2 nanocomposite photoelectrode was conceived and designed to convert CO_2 in aqueous methyl diethanolamine (MDEA) solution as the CO_2 absorption electrolyte.

2.0 Experimental methods

2.1 Materials

Graphite flakes with 7-10 μm nominal size were procured from Alfa Aesar. Tetra-n-butyl orthotitanate [$Ti(OBu)_4$] was procured from Sigma-Aldrich, and all other chemicals used in this work were of analytical grade. The indium tin oxide (ITO)-coated conducting glass plates (0.7 mm thickness) were procured from Osaka, Japan. Deionized water (18.2 MΩ cm) used in these experiments was from a Milli-Q system (Millipore, Bedford, MA; Mega-Pure System, Model MP-290). The carbon dioxide gas had 99.9% purity.

2.2 Preparation of reduced graphene oxide (RGO)

Graphene oxide (GO) was prepared by the modified Hummer's method [20]. Initially, 1 g of graphite flakes were mixed with sulfuric acid and phosphoric acid (120 mL:13 mL). Then, 6 g of $KMnO_4$ was added gradually, and the mixture was stirred continuously for 3 days. This was

followed by the addition of 7 mL of H_2O_2 solution (30%) and 135 mL of ice water until the mixture turned brown in color. The mixture was then centrifuged at 4000 rpm for 10 minutes. After centrifugation, the GO suspension was washed with 1 M HCl with sonication. The GO suspension was then dried in an oven and later subjected to hydrazine treatment to obtain the reduced graphene oxide (RGO) [21]. The GO powder (300 mg) was then added into 600 mL of ultrapure Milli-Q water and sonicated for 15 minutes. This was followed by the addition of 3 mL of hydrazine hydrate and the solution was stirred vigorously at 90 °C for 6 hours, precipitating the RGO as a black solid [21]. Finally the solution was filtered and washed with ethanol and water several times to obtain the RGO powder. The powder was dried in an oven at 80 °C.

2.3 Preparation of the Cu-RGO-TiO_2 nanocomposite

To prepare the TiO_2 nanocomposite, 20 mL of $Ti(OBu)_4$ (TBOT) was diluted in absolute ethanol and stirred continuously. Then, 6 mL of ultrapure water, 6 mL of ethanol, 1 mol% $Cu(NO_3)_2.5H_2O$ and 1 wt% RGO powder were mixed and sonicated for 1.5 hours. This mixture was added to the TBOT solution drop-wise for 30 minutes. Acetic acid was added to lower the pH of the solution to less than 3. The total mixture was vigorously stirred for 30 minutes to obtain a homogeneous solution. The dark colored solution was then stored at room temperature for 48 hours to complete the gel formation and was dried at 80 °C overnight. The dry porous gel was milled using a steel mortar and pestle. The fine powder catalyst was then calcined at 550 °C for 4 hours.

2.4 Fabrication of Cu-RGO-TiO_2/ITO photoanodes

The Cu-RGO-TiO_2 was deposited on the ITO substrate by electrophoretic deposition in a two-electrode cell. The prepared composite powder was dispersed in DI water with a concentration of 0.01 mg mL^{-1}. The pH of the solution was maintained by determining the zeta potential value. The composite powder mixture was sonicated in DI water to ensure a homogeneous dispersion before the electrophoretic deposition process.

2.5 Photoelectrochemical measurements

All photoelectrochemical measurements were performed in a cubic quartz photoelectrochemical cell using a potentiostat/galvanostat (Autolab PGSTAT30, Ecochemie, Netherlands). A standard three-electrode system was used, where the photoanode with an area of 1 cm^2 was the working electrode (WE). A platinum (Pt) wire and a saturated calomel electrode (SCE) were the counter (CE) and reference (RE) electrodes, respectively. The electrolyte in these experiments was 0.1 M Na_2SO_4. The potential in the voltammetric measurements was swept from 0.0 V to -1.5 V at 50 mV s^{-1}. Electrochemical impedance spectroscopy (EIS) was measured at the open circuit potential (OCP) both in dark and under solar irradiation. The EIS experimental data were simulated using analog circuits with NOVA 1.10 software on a computer interfaced with the potentiostat. The frequency range was from 10^{-1} Hz to 10^5 Hz with an acquisition of 10 points per decade and an amplitude of 5 mV around the OCP.

2.6 Constant potential photoelectrolysis

The photoelectrocatalytic conversion of CO_2 was performed in the quartz cell containing aqueous 10% methyl diethanolamine (MDEA). Figure 1 shows a schematic diagram of the

photoelectrocatalytic reduction process with a three-electrode system, where the CE and WE had the same surface area.

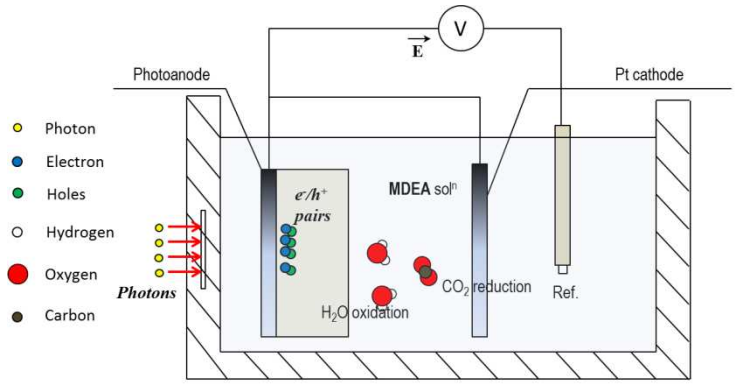

Figure 1: Quartz cell photoelectrocatalytic (PEC) reactor.

The irradiation intensity was ~10 mW cm^{-2}. Prior to the reaction, CO_2 was bubbled for 1 hour to saturate the solution, and the final pH of the CO_2-saturated solution was 7.6. The liquid phase product was analyzed by HPLC, and only the peaks for formic acid and methanol were considered.

2.7 Instrumentation

A scanning electron microscope (SEM, Quanta FEI 200) was used to study the morphology of the as-prepared composite samples. X-ray diffraction (XRD) was performed on a powder X-ray diffractometer (Bruker D8 Advance equipped with EVA diffract software, Germany) over a range of $10^{o} \leq 2\theta \leq 80^{o}$, at 40 kV and 30 mA with Cu Kα radiation (k = 1.5418 A^{0}). UV-Vis diffuse reflectance spectra were obtained on a Lambda 35 series equipped spectrophotometer (Perkin Elmer) with a thin film slot. Fourier transformed infrared spectroscopy (FTIR) was recorded by a Bruker IFS 66 V/S. The light source, a 150 W (Xe arc lamp) solar simulator, was from OSRAM photo optic (Germany). It had a consistent spectrum profile of AM 1.5G (i.e., similar characteristic features to a 1.5 global radiation solar light under

standard air conditions). X-ray photoelectron spectroscopy (XPS, Thermo Scientific K-alpha instrument) with an unmonochromatized Mg Kα radiation (photon energy 1253.6 eV) source, vacuum less than 10^{-9} Torr and spectral resolution of 0.1 eV, were carried out on flat gold (Si/10 nm Ti/200 nm Au) as the substrate and reference. The XPS core levels were aligned to the Au 4f 7/2 binding energy (BE) of 84 eV.

3.0 Results and discussions

3.1 Fabrication and characterization of the Cu-RGO-TiO_2/ITO composite electrode

The catalyst powder was characterized by crystallographic, imaging and optical techniques. Figure 2 shows the XRD pattern of the prepared catalyst. From the JCPDS ref. code 01-086-1157, the characteristic peaks at 25.3 (101), 37.9 (103), 48.1 (200), 53.9 (105) and 75.1 (215) are attributed to the titanium tetragonal system of the anatase phase.

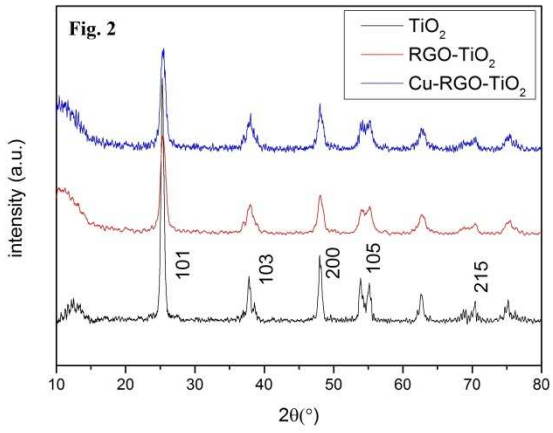

Figure 2: XRD of TiO_2, RGO-TiO_2 and Cu-RGO-TiO_2.

The calcination temperature of 550 °C played an important role in the production of the crystalline nanocomposites in the TiO_2 anatase phase. The phase change from anatase to rutile

was absent during the calcinations process. The Cu diffraction peaks at 2θ = 43º and 45º and Cu_2O peaks at 36º were not observed due to the low concentration and incorporation in the TiO_2 lattice structure. Figure 2 shows the overlap of the RGO characteristic peak at 25.8º with the TiO_2 (101) plane. Cu could be incorporated into the TiO_2 lattice due to the similarity of the Cu and Ti atomic radii (132 pm and 160 pm, respectively). Furthermore, the peaks attributed to Cu or Cu_2O were not observed. The average crystallite size is given by the Scherrer's formula (eq. 1):

$$D = \frac{K\lambda}{\beta cos\theta}, \quad (1)$$

where, D = crystallite size, λ = wavelength of the X-ray, β = full width at half maximum of the peak (in radians) and θ = angle of diffraction (in degrees). The average crystallite size of the Cu-RGO-TiO_2 composites (with respect to the anatase (101) peak) is between 15~28 nm. Thus, the doping of RGO did not introduce any crystalline phase changes, and we can conclude that RGO had no effect on crystallite size.

Figure 3 shows the XPS spectra of the Cu-doped TiO_2 nanoparticles. The electron-binding energy (BE) of the Ti 2p photoelectron peak (Fig. 3a) illustrates the existence of Ti^{4+} in the TiO_2 nanostructures at 458.2 eV. The oxygen peak at 529.5 eV (Fig. 3b) confirms the formation of the metal-oxygen bond, while the Cu 2p spectrum indicates the co-formation of Cu^{2+} and Cu^{+} in the structure (Fig. 3c). The binding energy of 932.2 eV is a characteristic of Cu_2O. The shake-up satellite peaks at 940.7 and 943.3 eV (green dashed lines) are an indication of Cu (II) formation [22, 23]. The existence of the shoulder (934.2 eV) in the copper spectrum also indicates the presence of Cu^{+} in the structure. The deconvoluted peaks in the copper spectrum indicate that 56% of the copper exists as Cu (I).

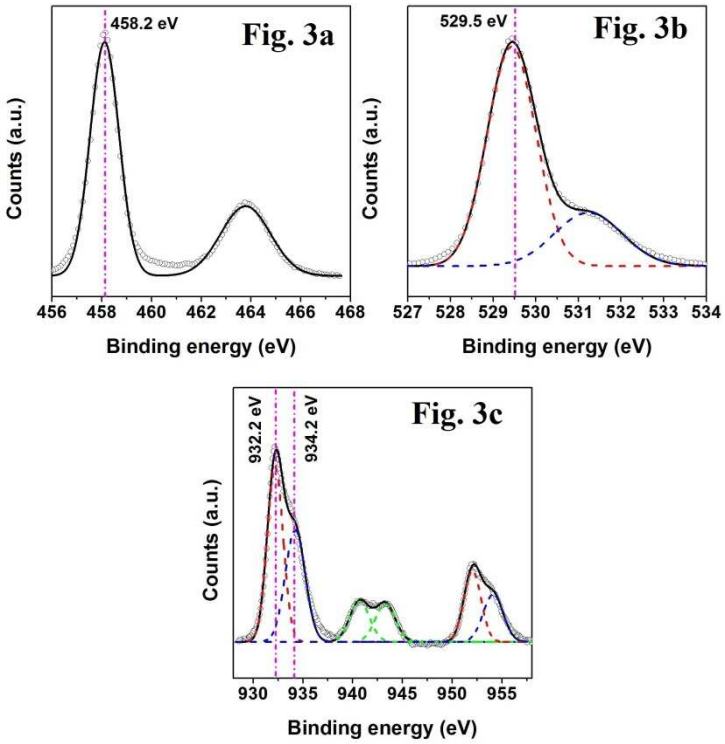

Figure 3: XPS spectra of Cu-doped TiO_2 nanoparticles: (a) Ti 2p, (b) O 1s and (c) Cu 2p.

Figure 4 shows the FESEM images of the thin film electrodes. The TiO_2 nanoparticles are quite homogeneous with sizes between 30-45 nm. The RGO-TiO_2 composites are also homogeneous, but more porous in the thin film form. The particle size varies within the same range as the TiO_2 nanoparticles, but the RGO-TiO_2 nanocomposites could be clearly distinguished from the single TiO_2 nanoparticles.

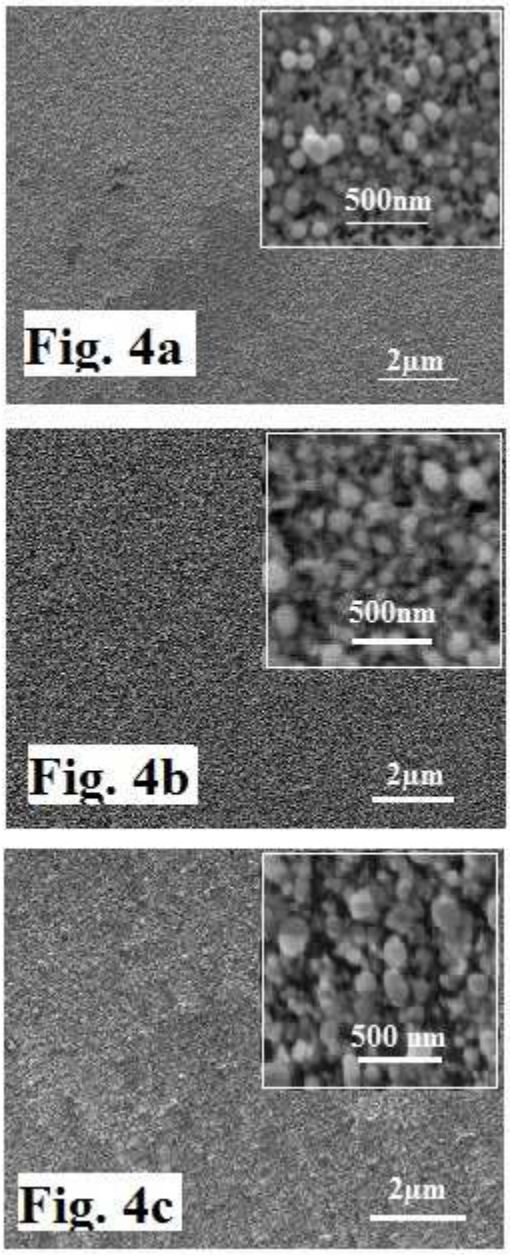

Figure 4: FESEM images of (a) TiO_2, (b) RGO-TiO_2 and (c) Cu-RGO-TiO_2.

A different morphology was observed for the Cu-RGO-TiO_2 thin film. The film bed is dense and packed, and the particle size is larger than the TiO_2 and RGO-TiO_2 nanoparticles. This morphological change could be due to the formation of grain boundaries at high calcination temperatures. Moreover, RGO has a tendency to aggregate into larger particles because of the weak Van der Waals interactions [24]. The RGO layers could not be clearly seen in the FESEM micrographs, which could be due to the charging effect of the electron-rich RGO [17, 25].

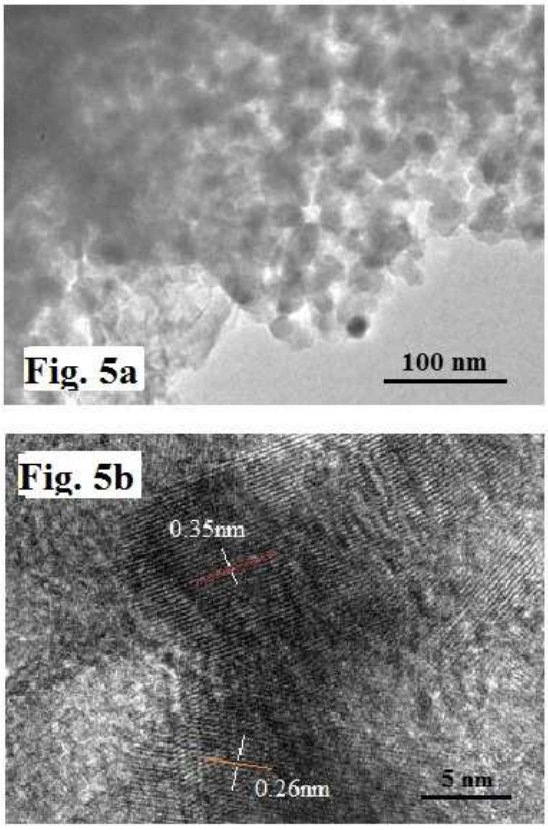

Figure 5: TEM image of Cu-RGO-TiO_2.

Figure 5 shows the HRTEM image of Cu-RGO-TiO_2**.** The estimated particle sizes (Fig. 5) are in good agreement with the XRD and SEM results. The relative d-spacing values resulted in successful Cu doping into the TiO_2 lattice. The Cu-RGO-TiO_2 film showed a slight red-shift in the absorbance edge and a significant enhancement of light absorption between 400-800 nm. Figure 6 shows the corresponding UV-Vis diffuse reflectance spectra of the fabricated thin films. The doping of Cu into the TiO_2 lattice creates intermediate sites for the transfer of photogenerated electrons, hence facilitates the electron-hole pair separation [26].

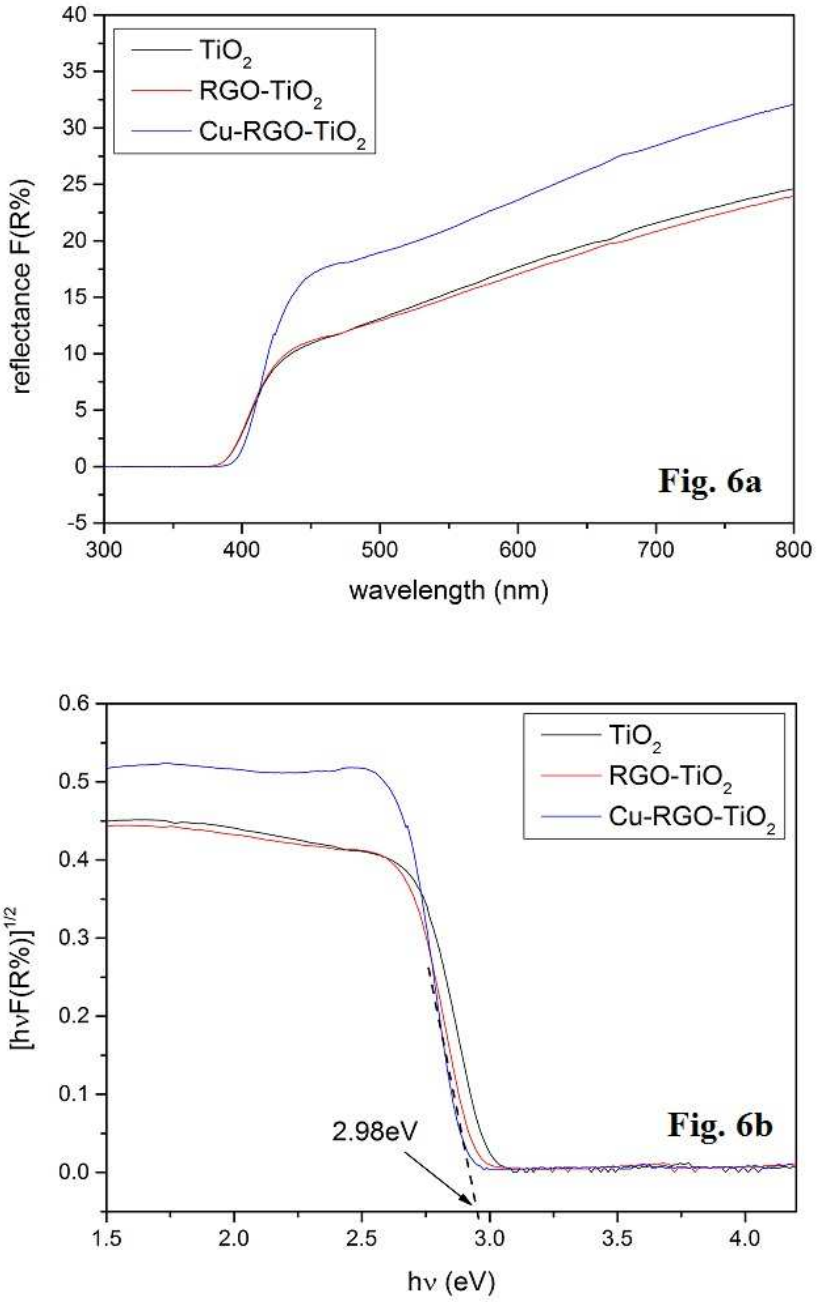

Figure 6: UV-Vis diffuse reflectance spectra of the TiO_2, RGO-TiO_2 and Cu-RGO-TiO_2 photocatalysts (a) and the plot of $\alpha h\nu^{1/2}$ *vs* $h\nu$ (b).

The incorporation of RGO, on the other hand, facilitates electron transfer and also increases the visible absorption of TiO_2. Thus, the doping of TiO_2 with Cu and incorporation of RGO are effective for enhanced photocatalytic activity. The optical band-gap was determined from the Kubelka-Munk equation as follows:

$$\alpha h\nu = A(h\nu - E_g)^n \quad (2)$$

where, α = absorption coefficient, A = constant (~1), v = frequency of light (3×10^8 ms^{-1}), h = Plank's constant (4.136×10^{-15} eV), E_g = band gap energy, n = 2 for indirect allowed transitions.

From equation (2) and the plot in 6(b), the E_g values of TiO_2, RGO-TiO_2 and Cu-RGO-TiO_2 are 3.23, 3.10 and 2.98, respectively. The lower band-gap of Cu-RGO-TiO_2 can be attributed to the formation of Ti-Cu-O, which lowers the conduction band level of TiO_2. The rapid recombination of the photogenerated electrons and holes emits photoluminescence (PL). A lower PL emission intensity indicates a decrease in the radiative recombination and better separation of the excitons [27]. Figure 7 compares the PL spectra of the prepared samples. Broad peaks were observed in the TiO_2 and RGO-TiO_2 samples between 500-700 nm. This indicates direct emission after excitation and poor separation of the photogenerated electrons and holes. The lower emission intensity of the Cu-RGO-TiO_2 sample could be due to the lower radiative combination of excitons, which indicates a slower recombination process.

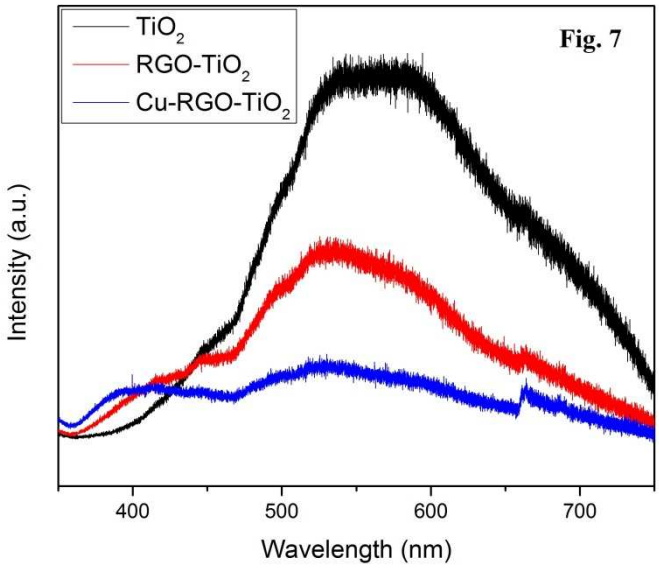

Figure 7: Photoluminescence spectra of TiO_2, RGO-TiO_2 and Cu-RGO-TiO_2.

The inclusion of Cu nanoparticles generates considerable fluorescence quenching indicative of efficient electron transfer from TiO_2 to Cu, due to the favorable electrical conduction between them. Under light irradiation, the excited electrons will follow the Cu-assisted path towards the RGO structure, which eventually decreases the direct recombination of the charge carriers.

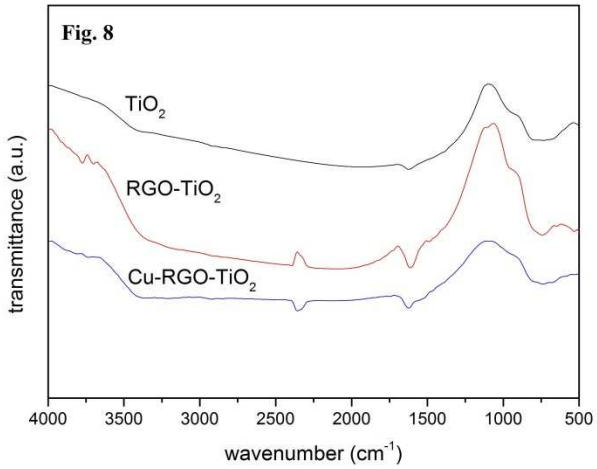

Figure 8: FTIR spectra of TiO_2, RGO-TiO_2 and Cu-RGO-TiO_2.

The FTIR spectra of the prepared catalyst samples are shown in Fig. 8. The prominent absorption bands are observed at 666, 1551 and 1626 cm^{-1}. In the RGO spectrum, most of the C=O bonds were eliminated, and the peak at 1720 cm^{-1} was absent, which confirms a well-reduced RGO structure. The peak at 1551 cm^{-1} is attributed to the graphene skeletal vibration. The Ti-O-Ti stretching vibrational peak is observed below 1000 cm^{-1}, and the broader peak in the 2400-3400 cm^{-1} range is attributed to the H-bonding between the –OH groups present on the TiO_2 surface [28]. A smaller peak at 2358 cm^{-1} could be due to the atmospheric CO_2 molecules adsorbed on the TiO_2 surface.

The most critical drawback in photoelectrocatalysis is the recombination process [29]. EIS is a useful tool to investigate the charge transfer and recombination processes at the semiconductor/electrolyte interface [30]. The EIS responses of TiO_2/ITO, RGO-TiO_2/ITO and Cu-RGO-TiO_2/ITO in the dark and under illumination are shown in the Nyquist plots (Fig. 9a).

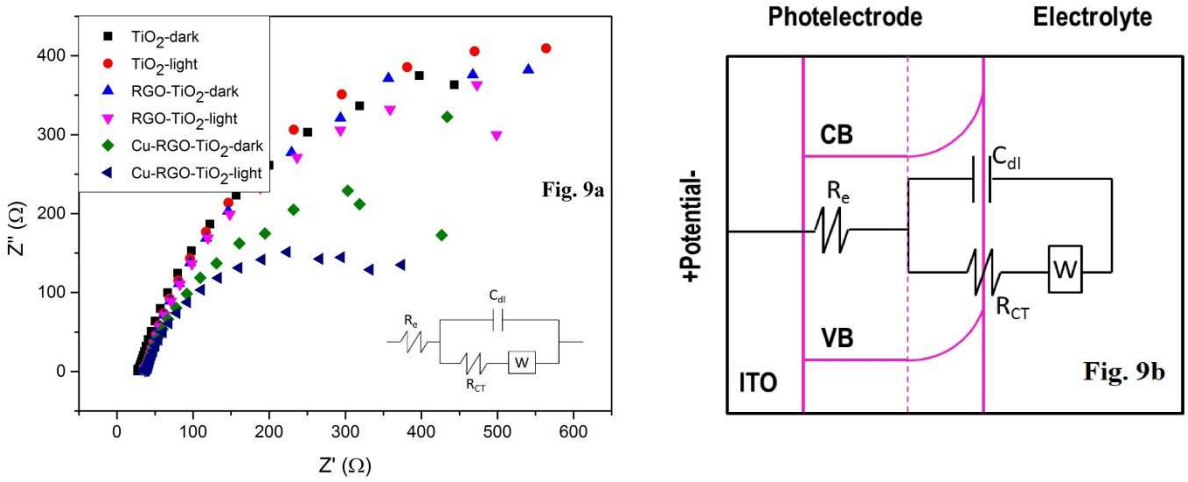

Figure 9: Nyquist plots of the TiO_2, RGO-TiO_2 and Cu-RGO-TiO_2 film electrodes at open circuit potentials both in the dark and under visible irradiation (9a) and conceptualization of the equivalent circuit model at the electrode-electrolyte interface (9b).

The impedance values of the photocatalysts were measured at the open circuit potential in dark and illuminated conditions. The Cu-RGO-TiO_2 thin film showed lower resistance than TiO_2 and RGO-TiO_2 under both conditions. Upon irradiation, the semicircle diameter decreases, and the charge transfer resistance (R_{CT}), which is the resistance of electron transfer process across the electrode/electrolyte interface, also decreases [31]. The inset of Figure 9a shows the equivalent circuit model across the electrode/electrolyte interface, where a Warburg diffusion model is proposed. Here, R_e refers to the bulk resistance between the WE and RE at the high frequency intercept of the semicircle with respect to the real axis. The interfacial resistance is represented by R_{CT} in the equivalent circuit model [32]. Figure 9b shows the equivalent circuit model which represents the electrode-electrolyte interface. Table 1 gives the R_{CT} values for all three photoelectrodes in both dark and irradiated conditions.

Table 1 The charge-transfer resistance (R_{CT}) of the TiO_2, rGO-TiO_2 and Cu-rGO-TiO_2 photoelectrodes from simulation of the EIS results.

Samples	Irradiation condition	R_{ct} / Ω cm^2
TiO_2	Dark	891.6
	Solar simulator	832.7
RGO-TiO_2	Dark	488.3
	Solar simulator	465.1
Cu-RGO-TiO_2	Dark	536.9
	Solar simulator	216.8

It can be observed that the Cu-RGO-TiO_2 electrode shows higher resistance (536.9 Ω cm^2) in the dark. This is probably due to the incorporation of Cu and corresponding defects in regular octahedral titania structure. But the charge transfer resistance decreases significantly (~217 Ω cm^2) upon irradiation,. This can be attributed to the electron channeling in the Ti-Cu-C structure which decreases the recombination of charge carriers and increases the photocurrent density. In fact, this proposed structure may have the rectifying characteristics due to the formation of Schottky barriers in the metal-semiconductor junction [33].

To investigate the effect of an applied bias on the modified TiO_2 photoelectrode, a Mott-Schottky plot was obtained at room temperature. The flat-band potential can be determined from the equation:

$$\frac{1}{C_{SC}^2} = \frac{2}{\varepsilon\varepsilon_0 q N_D}\left(V_B - V_{fb} - \frac{kT}{q}\right) \quad (3)$$

where, C_{SC} = space charge capacitance, V_{fb} = flat band potential, N_D = charge carrier conc. V_B = applied potential, ε is the dielectric constant of the semiconductor and ε_0 is the vacuum permittivity. Thus, the impedance measurement results can be plotted according to equation 3 and are shown in Fig. 10. The estimated flat-band potential and the corresponding donor density are -0.76V and 5.76×10^{15} cm^{-3}, respectively.

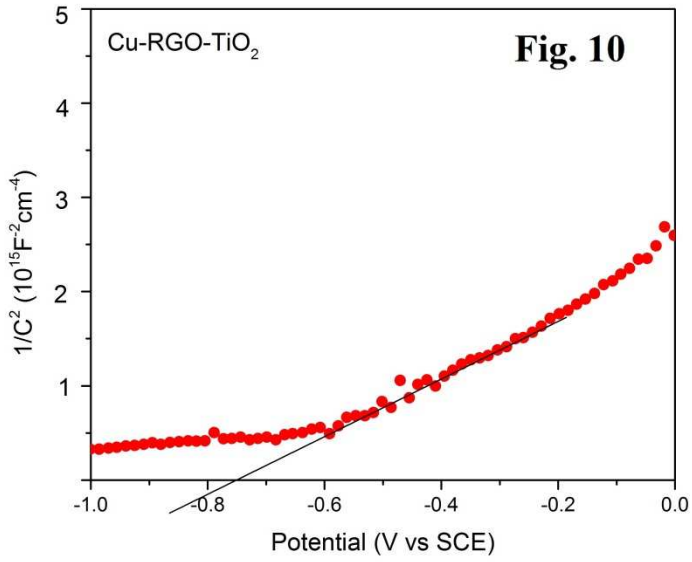

Figure 10: Mott-Schottky plot for Cu-RGO-TiO_2/ITO.

I should be noted that the onset potential for the anodic current is -0.82 V, and is not necessarily equal to the flat band potential. In fact, the flat band potential is a region where the recombination process tends to suppress the threshold of the photocurrent. Some factors i.e. crystallographic structure of TiO_2, doping, thin film properties etc. play a vital role in determining the flat band region. Hence the applied bias was chosen a little higher (-0.61V) than the estimated flat band potential to maintain the continuous flow of anodic photocurrent.

3.2 Photoelectrocatalytic reduction of carbon dioxide into formic acid and methanol

Figure 11 shows the voltammetric response of the catalyst films under illumination by the solar simulator. Prior to this, CO_2 gas was bubbled in the 10% MDEA solution for 1 hour to saturate the solution. No significant photocurrent was observed at the TiO_2/ITO and RGO-TiO_2/ITO electrodes. Moreover, blank experiments (without CO_2) were also carried out on all three electrodes and no photocurrent was observed in the process.

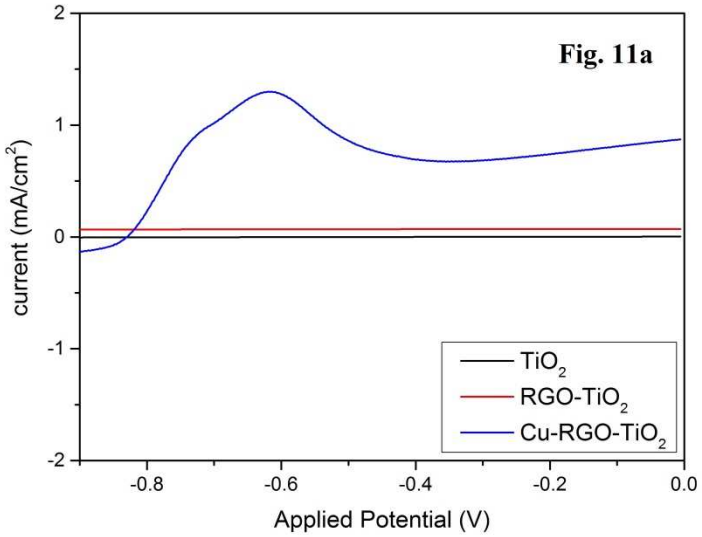

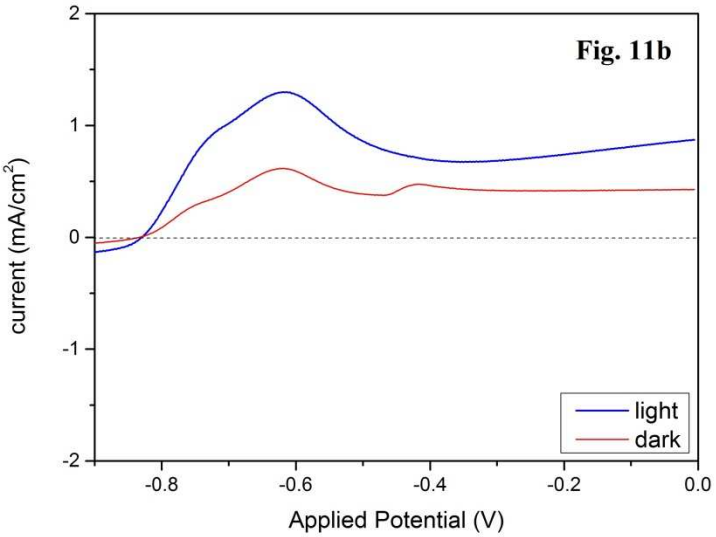

Figure 11: Voltammetry in 10% MDEA aqueous solution: (a) TiO_2, RGO-TiO_2 and Cu-RGO-TiO_2 electrodes under illumination and (b) the Cu-RGO-TiO_2 electrode in the dark and under illumination.

Cu-RGO-TiO_2 gives a maximum photocurrent of 1.31 mA cm^{-2} at -0.61 V vs. SCE. Figure 11b shows the effect of light and dark conditions of the Cu-RGO-TiO_2 photoelectrode in the CO_2-saturated solution. The photocurrent density was unsteady, and fluctuated during the reaction (Fig. 12a). In fact, CO_2 reduction process is a multi-electron transfer process and it is difficult to maintain the selectivity of a single product. Moreover, the competition between different electroactive species present in the electrolyte such as CO_2 and H^+ decreases the selectivity of the overall reaction. The interaction and catalytic effect of Cu atoms towards CO_2 in the electro-reduction process has been reported in earlier reports [34]. But pristine TiO_2 are not reactive with CO_2 molecules. This is probably due to the difficulties of the angular $CO^{\bullet}_2$ radicals to come in contact with the regular TiO_2 structure [35]. However, the initial photocurrent density is 4.56 mA cm^{-2} but decreases to 0.63 mA cm^{-2} at the end of the reaction. The slow diffusion process of CO_2 in the electrolyte may be responsible for the sudden decrease of photocurrent density and this can be understood from the impedance measurement Nyquist plots (Fig. 9a). This is evident by the appearance of the onset of a Warburg element at lower frequencies which denotes a diffusion limiting process for the Cu-RGO-TiO_2 electrode upon irradiation (Fig. 9a). A full photocurrent profile for a six-hour reaction period is shown in Fig. 12b.

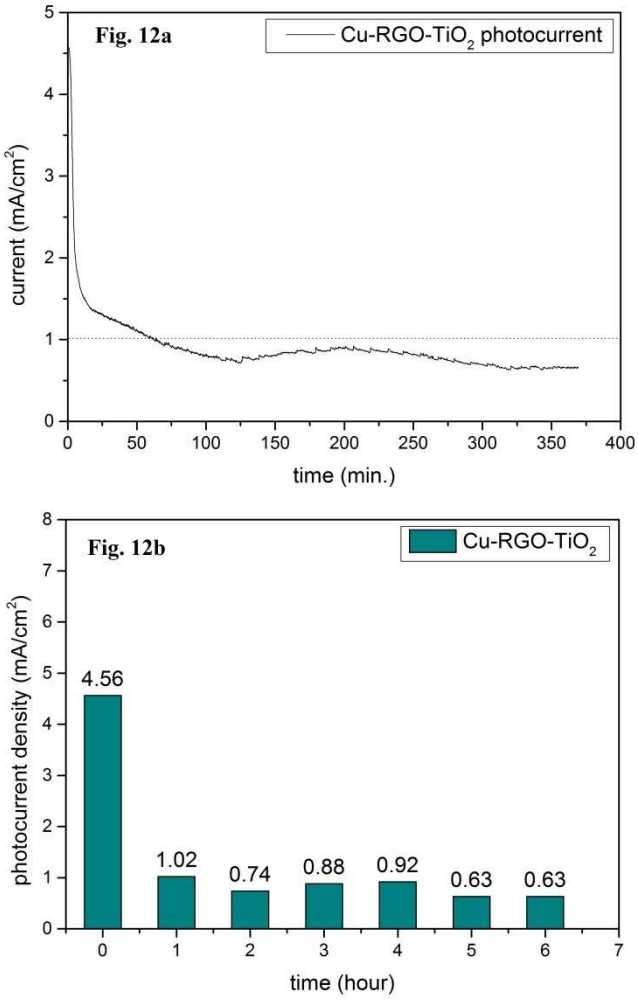

Figure 12: Cu-RGO-TiO_2 photoelectrode: (a) dependence of the photocurrent on reaction time in the photoelectrocatalytic reduction of CO_2 and (b) the photocurrent density profile for a six-hour reaction time.

3.3 Product analysis and efficiency

The products from the photoelectrolysis experiments were collected at one hour intervals. The saturated CO_2 solution in 10% MDEA contained an estimated concentration of 6950 ppm (~0.16 M) dissolved CO_2. After a six-hour period, the solution was analyzed, and the final concentrations of formic acid (fig. 13a) and methanol (fig. 13b) were 98 ppm and 242 ppm,

respectively. After 2 hours of reaction, the maximum formic acid concentration was 157 ppm, which decreased further (Fig. 13).

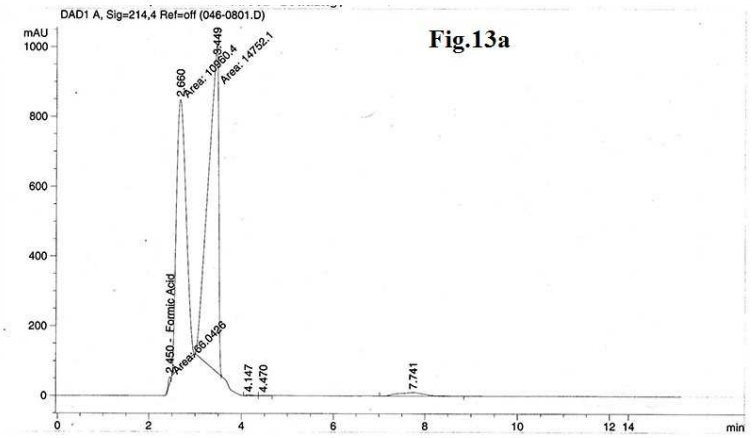

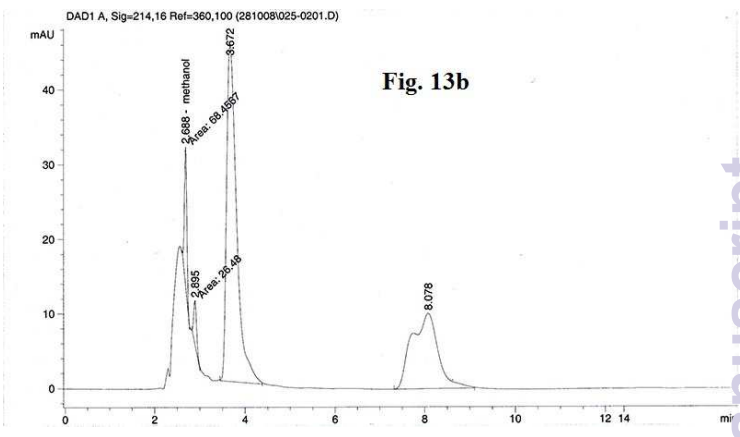

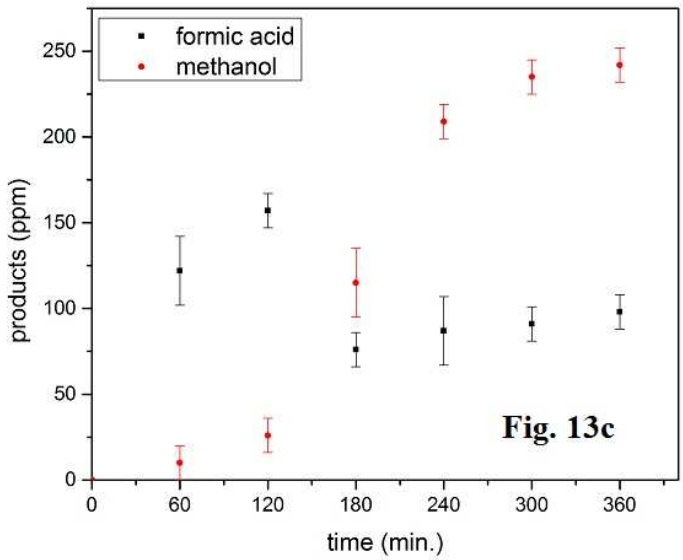

Figure 13: HPLC detection of (a) methanol and (b) formic acid, and (c) the yield of formic acid and methanol with time.

This could be due to the reduction of formic acid to methanol during the course of the reaction. The current efficiency was determined using Eq. 4 [36]:

$$Current\ Efficiency = \left[\frac{(IC)_0-(IC)_t}{8I\ \Delta t} \times FV\ 100\right]\%_{AM1.5G} \quad (4)$$

where $(IC)_0$ and $(IC)_t$ are the total organic carbon (g L^{-1}) at times 0 and t, respectively, I is the current (A), F is the Faraday constant (26.8 Ah), V is the volume (L) and *t* is the time of treatment (h). Thus, the estimated current efficiency for the process is 32.47%. Table 2 compares the literature results for the reduction of CO_2 to methanol and formic acid using TiO_2 photoelectrocatalysis and photocatalysis.

Table 2 Comparison of photocatalytic and photoelectrocatalytic reduction of CO_2 to methanol and formic acid on TiO_2 composites in the literature.

No	Electrode material / light source / solution	Catalytic method	Products	Highest yield	Ref.
1	Cu doped TiO_2, 8 W Hg lamp UVC (254 nm), CO_2 saturated 0.2 M NaOH.	Photocatalytic	Methanol	19.7 μmol g^{-1} h^{-1}	37, 38
2	Cu doped TiO_2, 10 W UV lamp, CO_2 saturated 1 M $KHCO_3$.	Photocatalytic	Methanol	450 μmol g^{-1} h^{-1}	39
3	Cu(I)/TiO_2 / 365 nm, 16 W/cm^2 UV, 1.2 wt.%-Cu/TiO_2 catalyst at 1.29 bar of CO_2 saturated pure water.	Photocatalytic	Methanol		40, 41
4	CdSe quantum dot (QD)-sensitized TiO_2 / visible light > 420 nm, CO_2 saturated pure water. 300 W Xe lamp.	Photocatalytic	Methanol	3.3 ppm g^{-1} h^{-1}	18
5	Cu-TiO_2 on molecular sieve 5A / UV light, CO_2 saturated 0.2 M NaOH. 250 W Hg lamp.	Photocatalytic	Methanol	0.78 μg h^{-1} g^{-1}	42
6	Pd nanoparticles Bismuth titanate, 0.1 CO_2 saturated H_2SO_4, solar simulator 300 W, 1.5 AM.	Photocatalytic	Formic acid	110-160 μmol h^{-1} g^{-1}	43
7	Nitrogen doped TiO_2. Cu counter electrode, CO_2 bubbled $KHCO_3$ electrolyte, 2V vs	Photo-electrocatalytic	Methanol Formic	Faradaic efficiency lower	10

	SCE. 100 W Xe lamp.		acid	than 8%.	
8	(CdS) and (Bi_2S_3) on TiO_2 nanotube. 500 W Xe lamp, wavelength less than 400 nm, CO_2 saturated 0.1 M NaOH, 0.1 M $NaSO_3$.	Photocatalytic	Methanol	44.9 μmol h^{-1} cm^{-2} (Bi_2S_3) 31.9 μmol h^{-1} cm^{-2} (CdS)	44
9	Cu-TiO_2-RGO, 0.1 M Na_2SO_4, CO_2 saturated 10% Methyl diethanolamine (MDEA), -0.61 V vs SCE. 150 W Xe arc lamp, 1.5 AM.	Photo-electrocatalytic	Methanol Formic acid	255 μmol h^{-1} cm^{-2} 189.06 μmol h^{-1} cm^{-2}	This work

The photo-oxidation of Cu-RGO-TiO_2 releases electrons and produces reactive holes, which react with water to release oxygen [45]:

Initial oxidation: $4\ h^+ + 2H_2O \rightarrow O_2 + 4H^+$

Initial reduction: $e^- + H^+ \rightarrow H^\bullet$ and $e^- + CO_2 \rightarrow {}^\bullet CO_2$

Subsequent reactions:

${}^\bullet CO_2 + 2H^\bullet + h^+ \rightarrow HCOOH$

${}^\bullet CO_2 + 6\ H^\bullet + h^+ \rightarrow CH_3OH$

A simple mechanism is shown in Fig. 14.

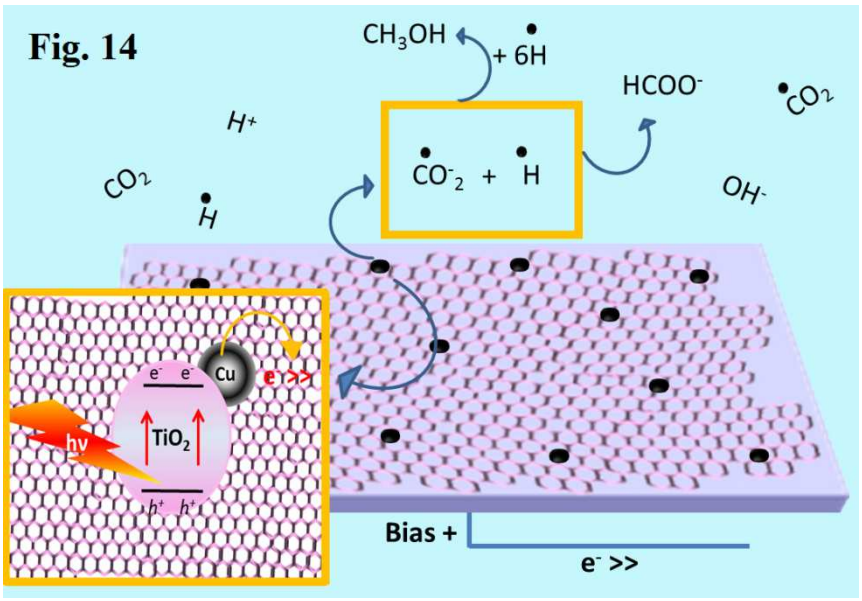

Figure 14: CO_2 photoelectrocatalysis mechanism in aqueous media.

4. Conclusions

Crystalline Cu-RGO-TiO_2 nanoparticles were prepared by sol-gel synthesis and deposited onto an ITO glass substrate via electrophoretic deposition. XRD and XPS analysis confirmed the incorporation of Cu dopant atoms into the TiO_2 lattice. Photo-absorption was observed in the visible region, and the band gap was 2.98 eV. The slow recombination of the photo-generated electrons and holes was confirmed by PL spectra. The composite WE was stable for more than 6 hours of reaction time. Formic acid (HCOOH) and methanol (CH_3OH) were the main products from the reduction of CO_2 with H_2O (or proton solvents) in MDEA solution, with rates of 255 µmol h^{-1} cm^{-2} and 189.06 µmol h^{-1} cm^{-2}, respectively. HCOOH was initially produced (maximum concentration of 157 ppm), but it later became an intermediate for the formation of

methanol and higher hydrocarbons. Cu doping directs the product selectivity towards HCOOH and CH_3OH and promotes the RGO-TiO_2 catalyst to produce larger amounts of CH_3OH (maximum 242 ppm) when the reaction time is more than 3 hours.

Acknowledgements

The authors would like to thank the University of Malaya for funding this work with High Impact Research (HIR-F-000032), RP005B 13AET and FP033 2013A research grants for their cordial support.

References

[1] A. Goeppert, M. Czaun, J.P. Jones, G.K.S. Prakash, G.A. Olah, Chem. Soc. Rev. 43 (2014) 7957-8194.

[2] W.N. Wang, Aerosol Air Qual. Res.. 14 (2014) 533-549.

[3] T. Yui, A. Kan, C. Saitoh, K. Koike, T. Ibusuki, O. Ishitani, ACS Appl. Mater. Interfaces, 3 (2011) 2594-2600.

[4] A. Dhakshinamoorthy, S. Navalon, A. Corma, H. Garcia, Energy Environ. Sci. 5 (2012) 9217-9233.

[5] Q. Zhai, S. Xie, W. Fan, Q. Zhang, Y. Wang, W. Deng, Y. Wang, Angew. Chem. Int. Edit. 52 (2013) 5776-5779.

[6] Z. Jiang, T. Xiao, V.L. Kuznetsov, P.P. Edwards, Philos. Trans. R. Soc. A, 368 (2010), 3343-3364.

[7] M. Halmann, Nature, 275 (1978) 115-116.

[8] T. Inoue, A. Fujishima, S. Konishi, K. Honda, Nature, 277 (1979) 637-638.

[9] Y. Wang, Q. Lai, F. Zhang, X. Shen, M. Fan, Y. He, S. Ren, RSC Adv. 4 (2014) 44442-44451.

[10] Y.P. Peng, Y.T. Yeh, S.I. Shah, C.P. Huang, Appl. Catal. B-Environ. 123-124 (2012) 414-423.

[11] Y.T. Liang, B.K. Vijayan, K.A. Gray and M.C. Hersam, Nano Lett. 11 (2011) 2865-2870.

[12] Z. Li, B. Gao, G.Z. Chen, R. Mokaya, S. Sotiropoulos, G.L. Puma, Appl. Catal. B-Environ. 110 (2011) 50-57.

[13] J.H. Yun, R.J. Wong, Y.H. Ng, A. Du, R. Amal, RSC Adv. 2 (2012) 8164-8171.

[14] C. Chen, W. Cai, M. Long, B. Zhou, Y. Wu, D. Wu, Y. Feng, ACS Nano, 4 (11) (2010) 6425-6432.

[15] K. Zhou, Y. Zhu, X. Yang, X. Jiang, C. Li, New J. Chem. 35 (2011) 353-359.

[16] L. Yuan, Q. Yu, Y. Zhang and Y.J. Xu, RSC Adv. 4 (2014) 15264-15270.

[17] M.R. Hasan, S.B.A. Hamid, W.J. Basirun, Z.Z. Chowdhury, A.E. Kandjani, S.K. Bhargava, New J. Chem. 39 (2014) 69-76.

[18] C. Wang, R.L. Thompson, J. Baltrus, C. Matranga, J. Phys. Chem. Lett. 1 (2010) 48-53.

[19] L.L. Tan, W.J. Ong, S.P. Chai, A.R. Mohamed, Nanoscale Res. Lett. 8 (2013) 465.

[20] D.C. Marcano, D.V. Kosynkin, J.M. Berlin, A. Sinitskii, Z. Sun, A. Slesarev, L.B. Alemany, W. Lu, J.M. Tour, ACS Nano, 4 (2010) 4806-4814.

[21] S. Stankovich, D.A. Dikin, R.D. Piner, K.A. Kohlhaas, A. Kleinhammes, Y. Jia, Y. Wu, S.T. Nguyen, R.S. Ruoff, Carbon, 45 (2007) 1558-1565.

[22] M.A. Mahmoud, W. Qian, M.A. El-Sayed, Nano Lett. 11 (2011) 3285-3289.

[23] N. Pauly, S. Tougaard, F. Yubero, Surf. Sci. 620 (2014) 17-22.

[24] M. Shi, J. Shen, H. Ma, Z. Li, X. Lu, N. Li, M. Ye, Colloid Surf. A-Physicochem. Eng. Asp. 405 (2012) 30-37.

[25] M.R. Hasan, S.B.A. Hamid, W.J. Basirun, Appl. Surf. Sci. doi: 10.1016/j.apsusc.2015.02.162.

[26] N.R. Khalid, E. Ahmed, Z. Hong, M. Ahmad, Y. Zhang, S. Khalid, Ceram. Int. 39 (2013) 7107-7113.

[27] J. Shi, J. Chen, Z. Feng, T. Chen, Y. Lian, X. Wang, C. Li, J. Phys. Chem. C, 111 (2007) 693-699.

[28] J. Shen, B. Yan, M. Shi, H. Ma, N. Li, M. Ye, J. Mater. Chem. 21 (2011) 3415-3421.

[29] X. Chen, S.S. Mao, Chem. Rev. 107 (2007) 2891-2959.

[30] F.F. Santiago, E.M. Barea, J. Bisquert, G.K. Mor, K. Shankar, C.A. Grimes, J. Am. Chem. Soc. 130 (2008) 11312-11316.

[31] W.H. Leng, Z. Zhang, J.Q. Zhang, C.N. Cao, J. Phys. Chem. B, 109 (2005) 15008-15023.

[32] X.I. He, Y.Y. Cai, H.M. Zhang, C.H. Liang, J. Mater. Chem. 21 (2011) 475-480.

[33] Z. Zhang, & J. T. Yates Jr., Chem Rev, 112(10) (2012) 5520-5551.

[34] Y. Hori, Springer New York, (2008) 89-189.

[35] V. P. Indrakanti, J. D. Kubicki, H. H. Schobert, *Fuel Processing Technology* (92) (2011) 805-811.

[36] T.T. Guaraldo, S.H. Pulcinelli, M.V.B. Zanoni, J. Photochem. Photobiol. A-Chem. 217 (2011) 259-266.

[37] I.H. Tseng, W.C. Chang, J.C.S. Wu, Appl. Catal. B-Environ. 37 (2002) 37-48.

[38] I.H. Tseng, J.C.S. Wu, H.Y. Chou, J. Catal. 221 (2004) 432-440.

[39] Slamet, H.W. Nasution, E. Purnama, S. Kosela, J. Gunlazuardi, Catal. Commun. 6 (2005) 313-319.

[40] J.C.S. Wu, H.M. Lin, C.L. Lai, Appl. Catal. A-Gen. 296 (2005) 194-200.

[41] J.C.S. Wu, H.M. Lin, Int. J. Photoenergy, 7 (2005) 115-119.

[42] B. Srinivas, B. Shubhamangala, K. Lalitha, P.A.K. Reddy, V.D. Kumari, M. Subrahmanyam, B.R. De, Photochem. Photobiol. 87 (2011) 995-1001.

[43] K.S. Raja, Y.R. Smith, N. Kondamudi, A. Manivannan, M. Misra, V. Subramanian, Electrochem. Solid State Lett. 14 (2011) F5-F8.

[44] X. Li, H. Liu, D. Luo, J. Li, Y.Huang, H. Li, Y. Fang, Y. Xu, L. Zhu, Chem. Eng. J. 180 (2012) 151-158.

[45] S. Ahmed, M.A. Mansoor, W.J. Basirun, M. Sookhakian, N.M. Huang, K.M. Lo, T. Söhnel, Z. Arifin, M. Mazhar, New J. Chem. 39 (2015) 1031-1037.